Chemical Science

ROYAL SOCIETY OF CHEMISTRY

EDGE ARTICLE

View Article Online
View Journal



Cite this: DOI: 10.1039/d6sc02057g

All publication charges for this article have been paid for by the Royal Society of Chemistry



# Surface engineering and local electron structure modulation to accelerate electroreduction of low-concentration nitrate

Zhifeng Gao,[a] Jianxing Liang,[bc] Mingdi Sun,[a] Xu Yin,[a] Haojie Ling,[a] Jiaxiu Wang,[a] Kajia Wei,[a] Kan Li*[b] and Weiqing Han*[a]

Received 12th March 2026
Accepted 26th May 2026

DOI: 10.1039/d6sc02057g

rsc.li/chemical-science

Electroreduction of low-concentration nitrate is constrained due to the competitive hydrogen evolution side reaction and sluggish reaction dynamics. Herein, we present a NiFe-layered double hydroxide featuring hydrophobicity and oxygen vacancies formed by *in situ* electrochemical intercalation of sodium dodecylbenzene sulphonate ($V_O$-NiFe-LDH/CF). Different from traditional intercalation by the ion-exchange method, $V_O$-NiFe-LDH/CF retains the hydrophobic properties of the alkyl chains in sodium dodecylbenzene sulphonate, while the sulfonic acid functional groups inhibit the formation of surface hydroxyl groups. The introduction of oxygen vacancies induces local electron redistribution and d-band center optimization, thereby enhancing nitrate adsorption capacity and reducing the energy barrier for the rate-determining step (*NO → *NOH). *In situ* FTIR measurement confirms the electrochemical hydrogenation route of nitrate. The optimized $V_O$-NiFe-LDH/CF can realize 96.8% nitrate removal efficiency and 96% ammonia selectivity at an initial $NO_3^-$-N concentration of 50 mg $L^{-1}$. The $NO_3^-$-N removal rate of $V_O$-NiFe-LDH/CF is 2.1-fold higher than that of NiFe-LDH/CF. Furthermore, $V_O$-NiFe-LDH/CF has excellent practicality for practical industrial nitrate-wastewater; the total nitrogen was reduced from 114.7 mg $L^{-1}$ to 7 mg $L^{-1}$. $V_O$-NiFe-LDH/CF shows outstanding stability and robust anti-interference performance during the long-term experiments.

## 1. Introduction

The electroreduction of nitrate to ammonia is a promising approach for sustainable nitrogen management, which is a "turning waste into wealth" strategy for ammonia production and the removal of $NO_3^-$-N contamination.[1,2] However, the electroreduction of low-concentration nitrate still suffers from competitive hydrogen evolution side reactions, particularly under acidic and neutral conditions. In addition, the process of nitrate conversion to ammonia is inherently constrained due to the requirement of multi-electron/proton transfer and the high energy barrier of the hydrogenation step. The design of durable and efficient electrodes is crucial for the electroreduction of low-concentration nitrate.

Layered double hydroxides (LDHs) are promising electrocatalysts for various electrocatalytic reactions due to their low cost, scalable synthesis and tunable composition.[3–6] LDHs are composed of positively charged brucite-like metal cation layers and interlayer galleries with charge compensating anions and water molecules. The metal cations are coordinated octahedrally by hydroxyl groups giving positively charged layers, and each hydroxyl group is oriented toward the interlayer region and may be hydrogen bonded to the interlayer anions and water molecules. Interestingly, due to the relatively weak interlayer bonding of LDHs, the controllable coordination environments of LDHs can be constructed by regulating the interlayer molecules. However, most of the previous research has focused on the modulation of interlayer spacing by various intercalations (*e.g.*, polyoxometalates, biomolecules and metal complex anions).[4] The NiFe LDH intercalated with dodecyl-sulfonate has exhibited stronger electrosynthesis activity for formaldoxime compared to that intercalated with $Cl^-$, in which the enhanced catalytic ability is attributed to the enlarged interlayer spacing of LDHs achieved by using different interlayer expansion agents.[7] The interlayer spacing of CoAl-LDH was enhanced from 0.76 to 1.33 nm by intercalation of sodium dodecyl sulfate, and the enlarged interlayer spacing enhanced the ion-diffusion channel.[8] However, the mechanism of local electron

[a]Key Laboratory of Chemical Pollution Control and Resources Reuse, School of Environmental and Biological Engineering, Nanjing University of Science and Technology, Nanjing, 210094, Jiangsu Province, PR China. E-mail: hwqnjust@aliyun.com

[b]State Key Laboratory of Green Papermaking and Resource Recycling, Shanghai Engineering Research Center of Solid Waste Treatment and Resource Recovery, School of Environmental Science and Engineering, Shanghai Jiao Tong University, 800 Dong Chuan Road, Shanghai, 200240, PR China. E-mail: likan@sjtu.edu.cn

[c]School of Chemistry and Chemical Engineering, Shanghai Jiao Tong University, 800 Dong Chuan Road, Shanghai, 200240, PR China

redistribution by regulating the interlayer molecules of LDHs is still unclear.

The water splitting reaction in the region of the cathode has a significant impact on the electroreduction process of nitrate. The balance between the generation and consumption of atomic hydrogen (*H) is crucial for the electrocatalytic hydrogenation of nitrate to ammonia.[9,10] Electrode surface engineering plays a pivotal role in the design of catalysts, as it directly influences nitrate enrichment, proton–electron transfer kinetics and water splitting behavior on the electrode surface.[11,12] Previous studies found that the hydrophobic interface significantly reduces $H^+$ concentration at the electrode surface compared to a hydrophilic interface, thereby effectively inhibiting the HER and utilizing *H for hydrogenation of nitrate.[13–16] Liu *et al.* reported that controllable interfacial wettability of a CNT electrode by altering the lengths of the alkyl chains in the surfactant allows fewer interfacial water molecules to reach the CNT surface, thereby significantly inhibiting the competitive HER and promoting $NH_3$ selectivity.[17] Therefore, the development of LDH cathodes with a hydrophobic surface by changing the interlayer molecules is a promising strategy for electroreduction of low-concentration nitrate.

In this work, we found that NiFe-LDH can simultaneously obtain abundant oxygen vacancies and a relatively hydrophobic surface only through adding sodium dodecylbenzene sulphonate (SDBS) during the electro-deposition process ($V_O$-NiFe-LDH/CF). The alkyl-chains of SDBS contribute to the hydrophobic properties, and the sulfonic acid functional groups of SDBS couple with metal cations inhibiting the formation of surface hydroxyl groups, resulting in the formation of oxygen vacancies. The optimized $V_O$-NiFe-LDH/CF electrode achieved 96.8% nitrate removal efficiency and 96% ammonia selectivity at an initial $NO_3^-$-N concentration of 50 mg $L^{-1}$. The nitrate removal rate of $V_O$-NiFe-LDH/CF is 2.1-fold higher than that of NiFe-LDH/CF without oxygen vacancies, while the hydrophobic electrode used in the traditional ion exchange method shows no significant improvement compared to NiFe-LDH/CF. This result indicated that the oxygen vacancies play an important role in the enhanced catalytic efficiency, and the hydrophobicity of the electrode reduces the accessibility of water molecules, thereby inhibiting the HER side reaction. The Bode phase plots and EPR spectra show that $V_O$-NiFe-LDH/CF maintains a good balance between generation and consumption of *H. The deoxygenation and hydrogenation process of electroreduction of nitrate was unveiled by *in situ* FTIR spectra. Density functional theory (DFT) calculations revealed that the introduction of oxygen vacancies resulted in an optimized d-band center, enhanced nitrate adsorption capacity and a reduced energy barrier of the rate-determining step (*NO to *NOH). Moreover, high $N_2$ selectivity (98.7%) was obtained in the presence of 1500 mg $L^{-1}$ $Cl^-$. Furthermore, $V_O$-NiFe-LDH/CF has excellent practicality for treating industrial nitrate-wastewater; the total nitrogen was reduced from 114.7 mg $L^{-1}$ to 7 mg $L^{-1}$. Consequently, the modulation of hydrophobicity and optimization of the local electronic structure to enhance the conversion efficiency of nitrate to ammonia on the surface of the electrode are highly effective. The unique design of a hydrophobic interface with oxygen vacancy synergy provides novel insights into regulating the nitrate–water interface environment and strategically designing advanced electrocatalysts for low-concentration nitrate wastewater treatment.

# 2. Experimental section

## 2.1 Materials

All chemicals used in this work were bought from commercial suppliers and used without further treatment. The detailed information is described in Text S1.

## 2.2 Preparation of $V_O$-NiFe-LDH/CF

The NiFe-LDH with oxygen vacancies was prepared on the copper foam by the *in situ* electrochemical intercalation method and named $V_O$-NiFe-LDH/CF (Fig. 1a). Briefly, the electrodeposition electrolyte comprised 0.459 g $FeSO_4 \cdot 7H_2O$, 0.97 g $Ni(NO_3)_2 \cdot 6H_2O$, 0.213 g $Na_2SO_4$ and 0.03 g SDBS ($C_{18}H_{29}NaO_3S$) which were dissolved in 50 mL deionized water. The electrodeposition process was carried out at a current density of 7.5 mA $cm^{-2}$ for 15 min in a two-electrode system where commercial Ir–Ru/Ti and the CF were used as the counter electrode and working electrode, respectively. The prepared electrodes were repeatedly washed with deionized water and ethanol three times and vacuum dried for 12 h at 60 °C.

For control experiments, NiFe-LDH/CF, $V_O$-Ni-LDH/CF and $V_O$-Fe-LDH/CF were prepared by following a similar procedure, except without the addition of SDBS, $FeSO_4 \cdot 7H_2O$ and $Ni(NO_3)_2 \cdot 6H_2O$, respectively. NiFe-LDH/CF-SC and NiFe-LDH/CF-SDS were prepared by following a similar procedure, except for replacing SDBS with sodium citrate (SC) and sodium dodecyl sulfate (SDS), respectively.

## 2.3 The experimental procedure for electrochemical nitrate reduction

Nitrate reduction experiments were carried out in a two-electrode system powered by a direct current power supply. The reaction tank was a 100 mL integrated electrolytic cell. As-prepared electrodes (2 × 3 $cm^2$) and commercial Ir–Ru/Ti (2 × 3 $cm^2$) were employed as the cathode and anode, respectively. The distance of two electrodes was set at 1.5 cm and 70 mL electrolyte including 50 mM $Na_2SO_4$ and 50 mg $L^{-1}$ $NO_3^-$-N was used. The reaction time was 3 h. If not specified, the applied current density is 10 mA $cm^{-2}$. Subsequently, 1.0 mL of electrolyte was collected at a 30-min interval and was quantitatively determined according to colorimetric methods through UV-vis absorption spectroscopy (Fig. S1) and the detailed measurement procedure is described in Text S2.

The $NO_3^-$-N removal ratio, $NH_4^+$-N generation ratio and selectivity ($R_{NO_3^-N}$, $G_{NH_4^+N}$ and $S_{NH_4^+N}$) were calculated using eqn (1)–(3):

$$R_{NO_3^-N}(\%) = \frac{[NO_3^-N] - [NO_3^-N]_t}{[NO_3^-N]_0} \times 100\% \quad (1)$$

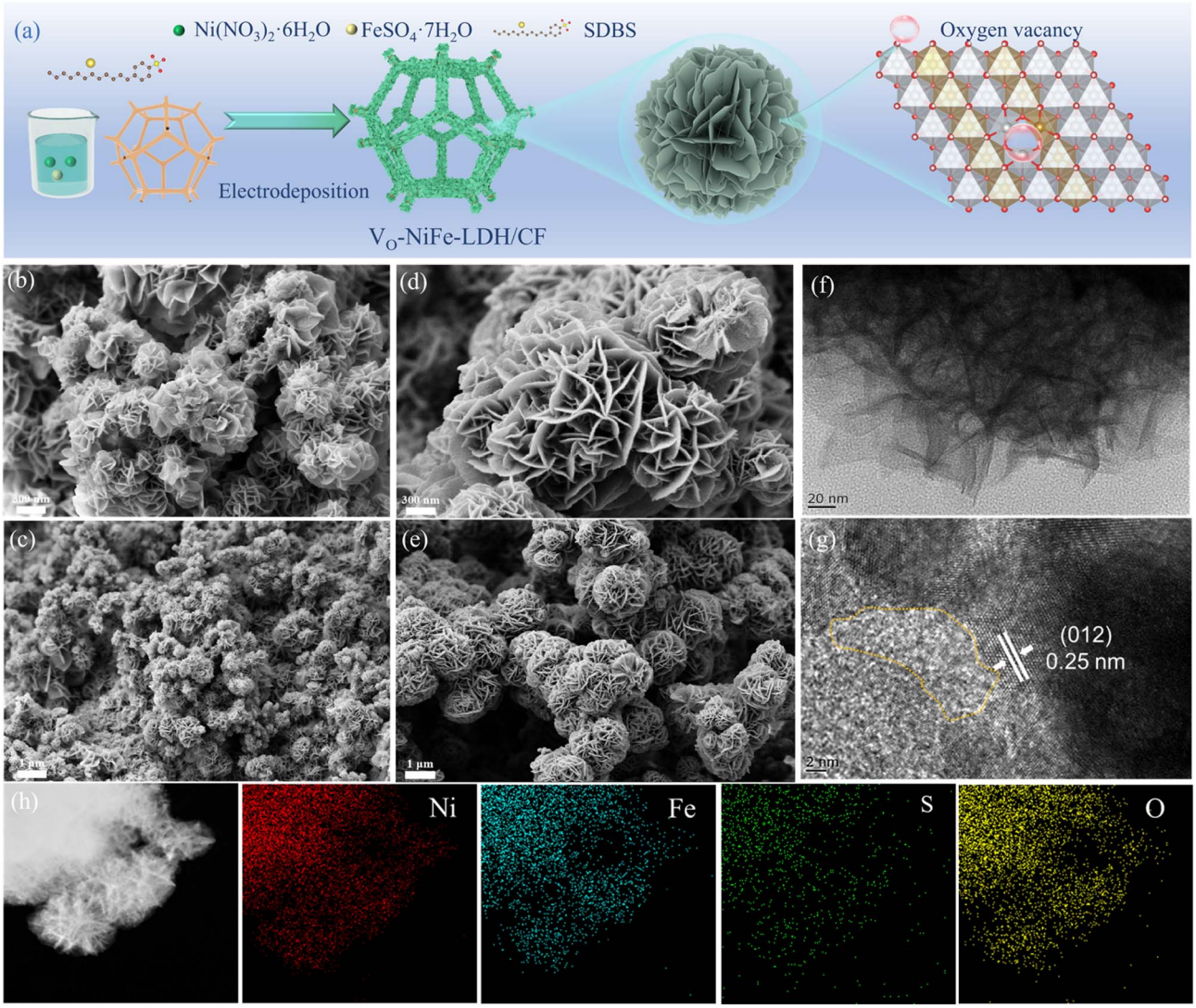


Fig. 1 (a) Schematic illustration of the $V_O$-NiFe-LDH/CF synthesis route. (b and c) SEM images of NiFe-LDH/CF and (d and e) $V_O$-NiFe-LDH/CF at different resolutions, (f and g) TEM image and HRTEM image, and (h) corresponding elemental mapping images of $V_O$-NiFe-LDH/CF.

$$G_{NH_4^+\text{-}N}(\%) = \frac{[NH_4^+\text{-}N]_t}{[NO_3^-\text{-}N]_0} \times 100\% \quad (2)$$

$$S_{NH_4^+\text{-}N}(\%) = \frac{[NH_4^+\text{-}N]_t}{[NO_3^-\text{-}N]_0 - [NO_3^-\text{-}N]_t} \times 100\% \quad (3)$$

where $[NO_3^-\text{-}N]_0$ is the initial concentration (mg $L^{-1}$) of $NO_3^-$-N. $[NO_3^-\text{-}N]_t$, $[NO_2^-\text{-}N]_t$, and $[NH_4^+\text{-}N]_t$ are the concentrations (mg $L^{-1}$) of $NO_3^-$-N, $NO_2^-$-N and $NH_4^+$-N at time $t$, respectively. The other calculations are described in Text S3.

### 2.4 Characterization and DFT calculations

The as-prepared electrodes were characterized by X-ray photoelectron spectroscopy (XPS), X-ray diffraction (XRD), Fourier transform infrared spectroscopy (FTIR), Raman microscopy, scanning electron microscopy (SEM), transmission electron microscopy (TEM) and Electron Paramagnetic Resonance (EPR). The electrochemical properties of electrodes were characterized using an electrochemical workstation (CHI 660E, Chenhua) with a three-electrode system with 50 mM $NaSO_4$ solution. The details are provided in SI Text S4.

All the computations were conducted based on the density functional theory (DFT) using the Vienna *Ab Initio* Simulation Package (VASP). The details are available in Text S5.

## 3. Results and discussion

### 3.1 Characterization of as-prepared cathodes

Fig. 1a illustrates the preparation process of $V_O$-NiFe-LDH on the Copper Foam (CF). All cathodes were prepared by a constant-current electrodeposition process with a fixed current density. Compared to the synthesis of NiFe-LDH/CF, SDBS was strategically introduced as an intercalating agent during the electrodeposition of $V_O$-NiFe-LDH/CF to simultaneously enhance hydrophobicity and construct oxygen vacancies. In previous study, SDBS was considered to affect the

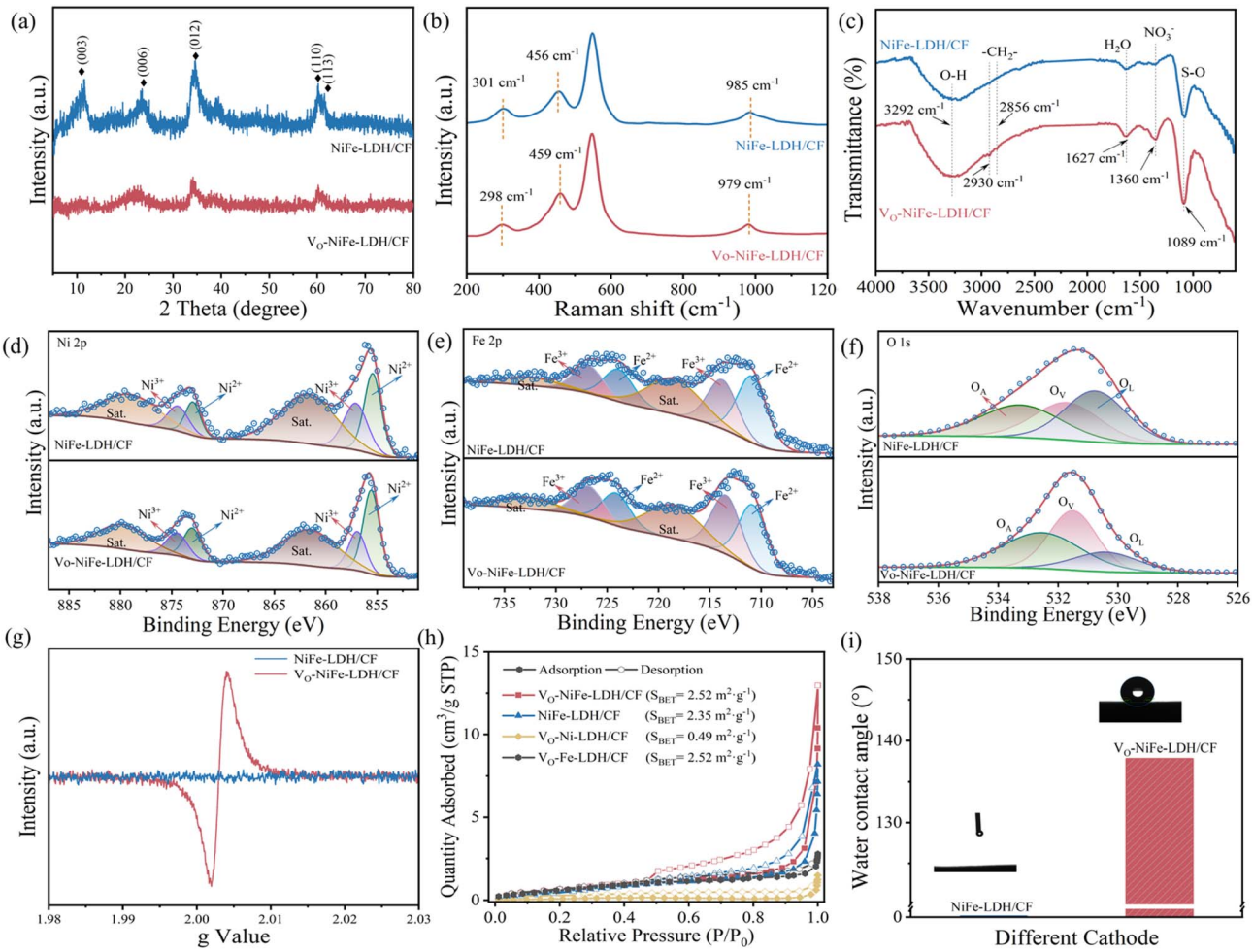


Fig. 2 (a) The XRD patterns, (b) Raman spectra, (c) FTIR spectra, (d–f) the Ni 2p, Fe 2p and O 1s XPS spectra, (g) EPR spectra, (h) $N_2$ adsorption–desorption isotherms of different electrodes and (i) water contact angle of NiFe-LDH/CF and $V_O$-NiFe-LDH/CF.

growth of crystals due to oriented aggregation based crystal growth.[18] The interaction between metal cations and surface hydroxyl groups is weakened due to the influence of the sulfonic groups of SDBS, resulting in the introduction of O vacancies in the LDH structure. As shown in Fig. 1b and c, the SEM images of NiFe-LDH reveal a nano-flower-like structure composed of single or multiple nanosheets stacked at 100–300 nm (Fig. 1d and e). The effect of morphology on catalytic performance was minimized in this study, in contrast to the finding reported by Wang *et al.*[8] In addition, the nanosheets of $V_O$-NiFe-LDH exhibit a smoother surface compared to those of NiFe-LDH. The results demonstrate that the introduction of SDBS enhances the coordination with metal ions, thereby facilitating the formation of nanosheets. The TEM images further confirm the hierarchical nano-flower-like structure composed of stacked nanosheets (Fig. 1f and S2). The high-resolution (HR-TEM) image (Fig. 1g) of $V_O$-NiFe-LDH/CF and the corresponding fast Fourier transform (FFT) pattern, inverse FFT (IFFT) image and line profile (Fig. S3a–c) confirm that the lattice spacing (0.25 nm) corresponds to the (012) crystal planes of hydrotalcite-like structure. In addition, lattice stripe fractures and discontinuities (marked by yellow dotted lines) can be clearly seen, which may be attributed to oxygen vacancies.[19] Elemental mapping of $V_O$-NiFe-LDH/CF demonstrates the uniform distribution of Ni, Fe, S and O throughout the catalyst (Fig. 1h).

As shown in Fig. S4, the diffraction peaks of metallic Cu at $2\theta$ = 43.3°, 50.4° and 74.1° correspond to the CF substrate (PDF#04-0836).[20] Additionally, XRD analysis of the sample scraped from the CF substrate confirms the formation of the NiFe-LDH phase (Fig. 2a). The diffraction peaks located at 11.79°, 23.77°, 34.74°, 60.28° and 61.66° are indexed to the (003), (006), (012), (110) and (113) reflections of the hydrotalcite-like structure of LDHs, respectively, demonstrating the successful synthesis of NiFe-LDH.[21] The reduced crystallinity of $V_O$-NiFe-LDH/CF can be ascribed to the fact that the interaction between metal cations and sulfonic groups of SDBS inhibited the growth of the LDH. The (006) diffraction peaks at 23.77° of NiFe-LDH shifted to 22.6°, suggesting the intercalation of SDBS. According to Bragg's law,[22] the *d*-spacing of *A* was calculated to be 0.75 nm and 0.79 nm, confirming the intercalation effect of SDBS. The characteristic peaks at approximately 548 and 456 cm$^{-1}$ in Raman spectra of NiFe-LDH/CF (Fig. 2b)

correspond to the $E_g$ bending mode and $A_{1g}$ stretching mode of M-OH species in the NiFe-LDH.[23,24] The shifted characteristic peaks were found in $V_O$-NiFe-LDH/CF, which indicated the electron transfer between Ni and Fe. The FTIR spectra of as-prepared electrodes were collected in the range of 400 to 4000 $cm^{-1}$ as shown in Fig. 2c. The characteristic peaks located at 3292 and 1627 $cm^{-1}$ were identified as the stretching vibration of OH groups and the bending vibration of adsorbed water molecules, respectively.[25] Characteristic vibration bands at 2930 and 2856 $cm^{-1}$ were observed, which are ascribed to the stretching vibration of the alkyl group in the long carbon chain structure of SDBS ions.[26,27] The results further reveal the presence of SDBS intercalation anions in the interlayer space. XPS was employed to characterize the elemental composition and electronic states of the as-prepared electrodes. The survey spectrum (Fig. S5) of $V_O$-NiFe-LDH/CF displays distinct elemental signals for Cu 2p, Ni 2p, Fe 2p, O 1s, C 1s and S 2p, with the S 2p peak intensity notably higher than that of NiFe-LDH/CF. The characterization results confirm the successful growth of NiFe-LDH on the CF substrate, while the enhanced S 2p signal intensity further validates SDBS intercalation within the LDH interlayers.[28] The Ni 2p spectrum of NiFe-LDH/CF can be deconvoluted into peaks of $Ni^{2+}$ (855.42 and 872.94 eV) and $Ni^{3+}$ (857.07 and 874.39 eV) along with satellite peaks at 861.67 and 878.97 eV, as shown in Fig. 2d. In Fig. 2e, the high-resolution Fe 2p XPS spectrum of NiFe-LDH/CF reveals two spin-orbit splitting peaks corresponding to Fe $2p_{3/2}$ and Fe $2p_{1/2}$, along with satellite peaks at 718.46 and 732.39 eV.[23] The peaks at 710.89 and 723.89 eV are ascribed to $Fe^{2+}$, while the peaks at 713.78 and 726.87 eV are assigned to $Fe^{3+}$. The peaks of Ni 2p and Fe 2p of $V_O$-NiFe-LDH/CF shift towards lower binding energy compared with that of NiFe-LDH/CF. The negative shift in the binding energy of Ni 2p and Fe 2p implies changes in the electron distribution, which can be attributed to the delocalized electrons originating from oxygen vacancies.[29] As shown in Fig. 2f, the peaks at 529.8, 531.6 and 532.3 eV corresponded to the lattice oxygen ($O_L$), oxygen vacancies ($O_V$) with low coordination and hydroxy groups from surface-absorbed water molecules ($O_A$), respectively.[30] In the O 1s XPS spectrum, $V_O$-NiFe-LDH/CF demonstrated a comparatively lower proportion of $O_L$ and a markedly higher intensity of $O_V$ when compared to NiFe-LDH/CF. This observation suggests the generation of extra oxygen vacancies within the $V_O$-NiFe-LDH/CF electrode. Solid-state EPR was performed to further confirm the formation of oxygen vacancies. An obviously asymmetric signal at $g = 2.003$ was observed after the addition of SDBS, which can be attributed to the unpaired electrons trapped in the oxygen vacancies (Fig. 2g). This finding further demonstrates the presence of oxygen vacancies.[31] Moreover, the S 2p spectrum of $V_O$-NiFe-LDH/CF is presented in Fig. S6. Furthermore, the specific surface area of as-prepared electrodes was investigated through $N_2$ adsorption–desorption experiments. The results indicated that $V_O$-NiFe-LDH/CF had a larger BET specific surface area compared to the other electrodes. In addition, the pore volume of the as-prepared electrodes was calculated as shown in Fig. S7. It was observed that there was an increased proportion of mesopores. The increased BET specific surface area and pore volume facilitate ion adsorption kinetics and enhance ion diffusion, thereby improving mass transfer efficiency.[8] The hydrophilicity of the electrodes was characterized by water contact angle measurements (Fig. 2i). The NiFe-LDH/CF electrode exhibited a water contact angle of nearly 0°, indicating its superhydrophilic properties. After SDBS intercalation, the water contact angle of $V_O$-NiFe-LDH/CF increased to 137.8°, demonstrating a significant transition to hydrophobicity.

### 3.2 Electrochemical nitrate reduction performance of as-prepared cathodes

The linear sweep voltammetry (LSV) curves of the $V_O$-NiFe-LDH/CF electrode are presented in Fig. 3a. A significantly increased current density and more positive onset potential were observed upon the addition of nitrate, demonstrating that nitrate electroreduction is preferentially promoted over the HER on the $V_O$-NiFe-LDH/CF electrode surface. The LSV curves of different electrodes were evaluated in a 50 mM $Na_2SO_4$ electrolyte with $NO_3^-$-N, further confirming the enhanced current response of $V_O$-NiFe-LDH/CF compared to the other electrodes (Fig. S8). Additionally, the electrochemically active surface area (ECSA) analysis revealed that $V_O$-NiFe-LDH/CF possesses a higher double-layer capacitance ($C_{dl}$) of 43 mF $cm^{-2}$ than the other electrodes, indicating a higher density of active sites after the introduction of oxygen vacancies (Fig. 3b, S9 and S10). $V_O$-NiFe-LDH/CF exhibits a significantly lower Tafel slope than the other electrodes, indicating faster reaction kinetics (Fig. S11). As shown in Fig. 3c and S12, the electrochemical impedance spectroscopy (EIS) results reveal the smallest charge transfer resistance for $V_O$-NiFe-LDH/CF, demonstrating its superior charge transfer efficiency compared to the other electrodes. These electrochemical characterization studies demonstrate that $V_O$-NiFe-LDH/CF exhibits the highest intrinsic catalytic activity among all prepared electrodes, indicating that the intercalation of SBDS effectively enhances the electrochemical activity of the electrode. To further evaluate the nitrate reduction performance of the as-prepared electrodes, electrochemical nitrate reduction tests were conducted in a two-electrode system with a current density of 10 mA $cm^{-2}$, using an aqueous electrolyte containing 50 mM $NaSO_4$ and 50 mg $L^{-1}$ $NO_3^-$-N. As shown in Fig. 3d–f, the CF substrate exhibits a negligible catalytic activity for $NO_3^-$-N removal and $NH_4^+$-N generation, indicating that the contribution of the substrate to nitrate-to-ammonia conversion is almost negligible in this reaction system. $V_O$-NiFe-LDH/CF exhibits a significantly higher $NO_3^-$-N removal capacity (96.8% after 180 min of electrolysis) compared to the other electrodes. Furthermore, the $NO_3^-$-N removal rate of $V_O$-NiFe-LDH/CF (0.01375 $min^{-1}$) is 14.3, 6.5 and 2.1 times higher than those of $V_O$-Fe-LDH/CF (0.00096 $min^{-1}$), $V_O$-Ni-LDH/CF (0.00213 $min^{-1}$) and NiFe-LDH/CF (0.00656 $min^{-1}$), respectively. $V_O$-NiFe-LDH/CF exhibits excellent selectivity for $NH_4^+$-N (96%) and a lower generation ratio of $NO_2^-$-N compared to the other electrodes. It is worth noting that the generation ratio of $NO_2^-$-N in the $V_O$-NiFe-LDH/CF system remains within a relatively lower range (Fig. S13). To avoid measurement error of UV-vis detection, we further performed ion chromatography

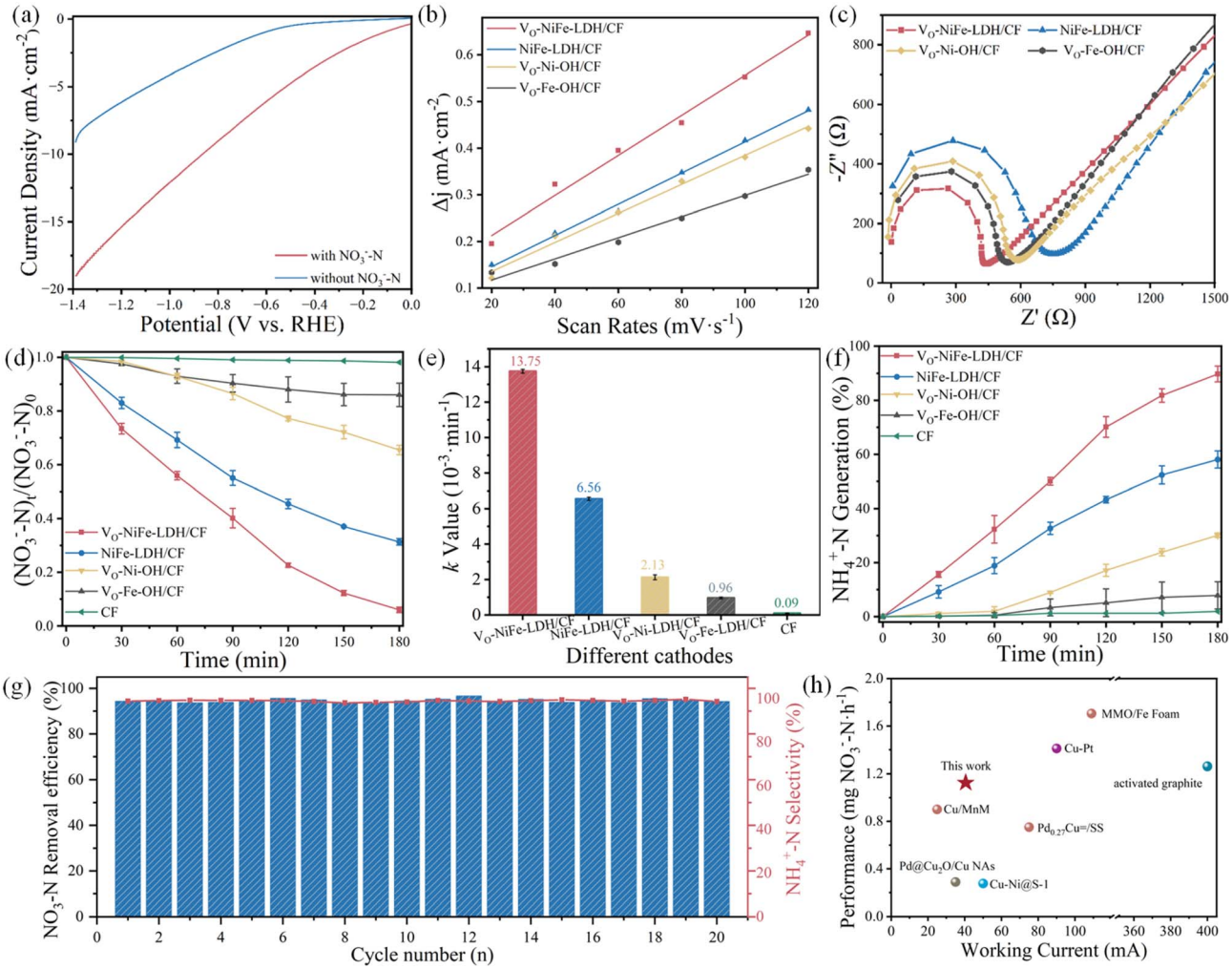


Fig. 3 (a) LSV curves of $V_O$-NiFe-LDH/CF with and without $NO_3^-$-N, (b) linear fitting of the capacitive properties of current density *vs.* scan rate, (c) EIS Nyquist plots, (d–f) the performance (the removal ability and kinetic rate constant of $NO_3^-$-N removal and $NH_4^+$-N generation ratio) of electrochemical nitrate reduction of different electrodes, (g) the stability tests and (h) comparison of reported electrodes for low-concentration nitrate removal at constant working current.

(IC) tests on the same samples. As shown in Fig. S14, the results obtained from UV-vis and IC measurements are in good agreement, with only minor discrepancies between the two methods. To further investigate the stability of $V_O$-NiFe-LDH/CF, continuous electrolysis experiments with the $V_O$-NiFe-LDH/CF cathode are presented in Fig. 3g, and the $NO_3^-$-N removal efficiency shows no significant attenuation during the 20 cycling experiments. Additionally, Ni and Fe leaching concentrations remained below 0.01 mg $L^{-1}$ throughout the operation, further confirming the excellent long-term stability of the $V_O$-NiFe-LDH/CF cathode (Fig. S15). After long-time cycling experiments, $V_O$-NiFe-LDH/CF hardly changed and still retained a nano-flower-like structure (Fig. S16). Notably, the post-reaction XPS results show that the relative concentration of oxygen vacancies decreases from 56.5% (fresh electrode) to 48.8% (used electrode) (Fig. S17). This phenomenon can be attributed to the adsorption of reaction intermediates, which increases the proportion of $O_A$ and thus reduces the relative content of $O_v$. This result is consistent with the reported literature.[32] Furthermore, the XPS spectra of Fe 2p and Ni 2p show no obvious variation after long-term cycling experiments, further confirming the excellent structural stability of $V_O$-NiFe-LDH/CF. Additionally, compared with some reported electrodes synthesized by the *in situ* growth method, $V_O$-NiFe-LDH/CF exhibits a better performance in low-concentration nitrate removal at constant working current.[33–39] As shown in Fig. 3h, $V_O$-NiFe-LDH/CF has a stronger removal ability of $NO_3^-$-N at relatively lower working current, which indicated that it may have promising industrial application prospects.

### 3.3 Electroreduction mechanism of nitrate over $V_O$-NiFe-LDH/CF

In order to determine the role of oxygen vacancies and surface hydrophobicity in the electroreduction of nitrate, we have added two additional control electrodes. A hydrophilic LDH with a comparable oxygen vacancy concentration (NiFe-LDH/

CF-SC) was synthesized using sodium citrate (SC) as the intercalating agent, while a hydrophobic LDH without oxygen vacancies (NiFe-LDH/CF-SDS) was prepared with sodium dodecyl sulfate (SDS) as the intercalating agent. SC induces oxygen vacancies mainly through the chelation of its hydroxyl and carboxyl groups with metal ions of LDH. This interaction disturbs the local coordination environment and causes lattice distortion, thereby generating unsaturated coordination sites and eventually leading to the formation of oxygen vacancies. By contrast, SDS undergoes directional adsorption and hydrophobic self-assembly *via* its long alkyl chains, solely endowing the electrode with surface hydrophobicity. Owing to the absence of strong electron-withdrawing groups that induce defects, SDS does not facilitate the formation of oxygen vacancies. The surface wettability and oxygen vacancy defects of the as-prepared electrodes were systematically characterized, as displayed in Fig. S18. As shown in Fig. S19, $V_O$-NiFe-LDH/CF exhibits a higher removal capacity of $NO_3^-$-N than the other electrodes. Both NiFe-LDH/CF-SC and NiFe-LDH/CF-SDS also outperform NiFe-LDH/CF. Furthermore, NiFe-LDH/CF-SC exhibits better catalytic performance than NiFe-LDH/CF-SDS, indicating that oxygen vacancies play a more dominant role than surface hydrophobicity in the electrocatalytic nitrate reduction process. $V_O$-NiFe-LDH/CF exhibits a higher faradaic efficiency (44.2%) and $NH_3$ yield rate than the other control electrodes (Fig. S20), and the energy consumption for $NH_3$ is 2.17 kWh $mol^{-1}$. To further investigate the catalytic mechanism of $V_O$-NiFe-LDH/CF, *operando* EIS and DFT calculations were employed to study the reaction kinetics of water dissociation, nitrate activation and the reduction process.[40–42] Differential charge density analysis reveals stronger electron transfer at the $V_O$-NiFe-LDH and $*NO_3$ interface compared to NiFe-LDH (Fig. 4a), demonstrating that oxygen vacancies induce the local electron redistribution. The Bader charge analysis revealed that the $V_O$-NiFe-LDH transferred 0.39 electron equivalents to $NO_3^-$, significantly higher than the values for NiFe-LDH (0.25). As shown in Fig. S21, the conversion efficiency of nitrate-to-ammonia is inhibited after the TBA addition. Control experiments were performed by replacing $H_2O$ with deuterium oxide ($D_2O$) to clarify the role of *H, since *H originated from the electrochemical splitting of $H_2O$. The current densities of LSV curves decreased when $D_2O$ was used instead of $H_2O$ (Fig. S22a), and the kinetic isotope effect (KIE) value of $V_O$-NiFe-LDH/CF is 1.64 (Fig. S22b), demonstrating that *H plays a critical role in the electrochemical reduction of $NO_3^-$-N. Furthermore, $V_O$-NiFe-LDH/CF exhibits stronger DMPO-*H adduct peaks than NiFe-LDH/CF, and the peak intensity decreases after the addition of nitrate, suggesting that $V_O$-NiFe-LDH/CF has an enhanced ability for *H generation and consumption (Fig. 4b). Fig. 4c presents the Bode phase plots of $V_O$-NiFe-LDH/CF at different working potentials. In the absence of nitrate, the Volmer step (water dissociation process) is the dominant reaction. A positive shift of peak position with increasing potential is observed, indicating enhanced water dissociation kinetics and increased *H generation. Upon application of a sufficiently large potential, the peak exhibits a distinct shift toward the middle frequency range, thereby accelerating the Heyrovsky step for the HER.[43] After nitrate addition, significant decreases in peak intensity and notable shifts in peak position toward higher frequency are observed, confirming that the suppressed Heyrovsky step and generated *H species are preferentially consumed for the nitrate reduction hydrogenation step compared to the HER. In Fig. S23a, $V_O$-NiFe-LDH/CF exhibits a significantly lower peak intensity than NiFe-LDH/CF, with peaks shifting to higher frequency at increasingly negative applied potential. These results indicate that the Volmer step has achieved dynamic equilibrium, and H* generated from water dissociation is preferentially consumed at the $V_O$-NiFe-LDH/CF surface during the nitrate reduction, thereby promoting the hydrogenation of nitrate to ammonia.[44] Additionally, the peak position of $V_O$-NiFe-LDH/CF shifts toward lower frequency in the middle frequency range ($10^0$–$10^2$ Hz) compared with the other electrodes, further confirming that oxygen vacancy introduction and bimetallic collaboration can effectively suppress the Heyrovsky step, thereby inhibiting the HER side reaction (Fig. S23b). Furthermore, Fig. 4d presents the calculated projected density of states (PDOS) and corresponding d-band centers for $V_O$-NiFe-LDH (−2.29 eV) and NiFe-LDH (−3.08 eV), revealing distinct electronic structure differences induced by oxygen vacancies. A positive shift of the d-band center for $V_O$-NiFe-LDH is closer to the Fermi level compared to NiFe-LDH, which is beneficial for the adsorption of nitrate and the intermediates.[45] The calculations of *H free energy on the different electrocatalysts (Fig. 4e) demonstrate enhanced adsorption ability of *H, thereby promoting the hydrogenation steps in nitrate-to-ammonia conversion. *In situ* FTIR spectra were collected to monitor the intermediates adsorbed on the surface of the electrode (Fig. 4f and S24). The characteristic peak at around 1340 $cm^{-1}$ could be attributed to the vibration of $*NO_3^-$.[42] The characteristic peaks of the protonation intermediates were found, including –N–H (2850 and 2951 $cm^{-1}$),[46] *NH (1558 $cm^{-1}$), *NHOH (1525 $cm^{-1}$)[47,48] and the product $NH_4^+$ (at around 1457 and 1507 $cm^{-1}$),[49] while the band at 1652 $cm^{-1}$ is attributed to *NO.[50] The relative peak intensity ratio of *NHOH *versus* *NO species gradually increased with increasing working potential, demonstrating the hydrogenation pathway of nitrate reduction. Moreover, the ratio over $V_O$-NiFe-LDH/CF was significantly higher than that over NiFe-LDH/CF at the same working potential, further revealing the promoted hydrogenation kinetics. In addition, the adsorption free energy of the $NO_3^- \rightarrow *NO_3$ process is identified as the prerequisite rate-determining step in the overall nitrate reduction reaction. The adsorption energy of $NO_3$ decreases from 0.14 eV to −0.54 eV, indicating that the energy barrier of the prerequisite step is overcome and the reaction shifts toward a thermodynamically favorable spontaneous process. The enhanced nitrate adsorption ability of $V_O$-NiFe-LDH/CF was evaluated using electrochemical impedance-potential spectra at different nitrate concentrations (Fig. S25 and S26). The enhanced specific adsorption of $NO_3^-$ on $V_O$-NiFe-LDH/CF was proved according to the Esin–Markov effect on the inner Helmholtz plane.[51] The result is in favor of the successive deoxidation and hydrogenation steps. The Gibbs free energy profiles of the nitrate to ammonia on NiFe-LDH and $V_O$-NiFe-LDH are presented in

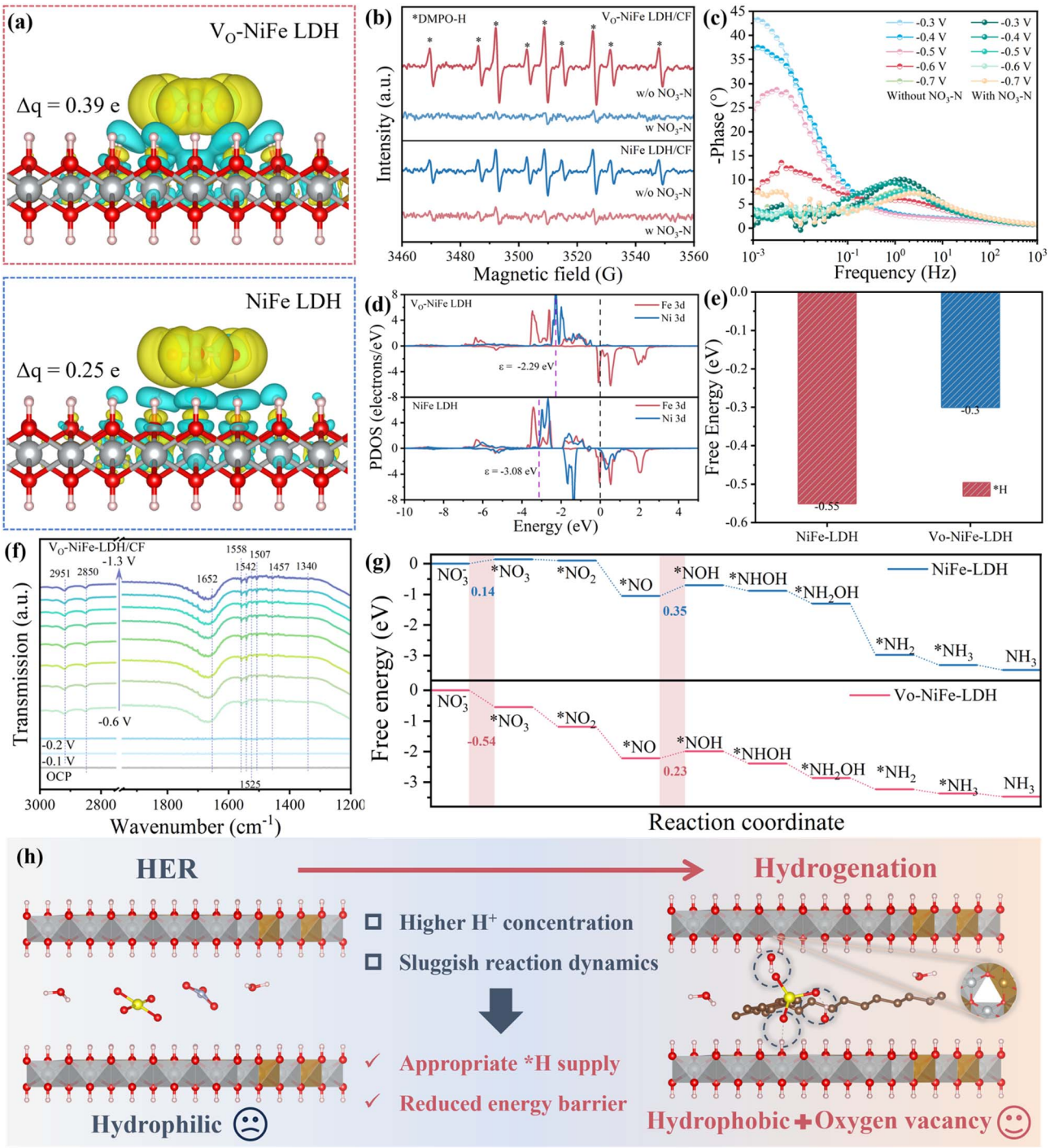


Fig. 4 (a) The charge density difference diagram and Bader charge of $NO_3^-$ adsorption on the $V_O$-NiFe-LDH and NiFe-LDH. (b) EPR spectra of DMPO-*H during the electrocatalysis process. (c) The potential-dependent Bode plots of $V_O$-NiFe-LDH/CF. (d) The PDOS of d-bands, (e) the adsorption free energy of H and (f) *in situ* FTIR spectra of $V_O$-NiFe-LDH/CF. (g) The Gibbs free energy change of the $NO_3$RR over NiFe-LDH and $V_O$-NiFe-LDH (where * denotes the active site on the catalyst surface). (h) Schematic diagram of enhanced electroreduction ability of low-concentration nitrate over $V_O$-NiFe-LDH/CF.

Fig. 4g. The nitrate to ammonia process can be considered a direct reduction process in combination with electron transfer and N–H bonding. The nitrate reduction reaction proceeds through a series of intermediates with N valences ranging from +5 to −3: $NO_3^-$ → *$NO_3$ → *$NO_2$ → *NO → *NOH → *NHOH → *$NH_2OH$ → *$NH_2$ → *$NH_3$ → $NH_3$. DFT calculations reveal that the *NO → *NOH step is the rate-determining step for NiFe-LDH in the whole process. The presence of oxygen vacancies reduces the reaction energy barrier of *NO → *NOH (0.23 eV) compared to NiFe-LDH/CF (0.35 eV). In summary, to

address the competitive HER and sluggish reaction dynamics associated with the removal of low-concentration nitrate, we proposed a strategy of adding SDBS during LDH electrode deposition to introduce oxygen vacancies. The strategy regulates the surface hydrophobicity and local electronic structure of the electrode, thereby enabling appropriate *H supply and reducing the energy barrier of the hydrogenation process (Fig. 4h).

### 3.4 The application potential of $V_O$-NiFe-LDH/CF

To further investigate the practicability of $V_O$-NiFe-LDH/CF, a series of electrochemical nitrate reduction experiments were conducted using various operational parameters, including SDBS dosage in the electrodeposition process, working current density, initial pH, initial $NO_3^-$-N concentration and different interfering ions. As shown in Fig. 5a, b, S27 and S28, both $NO_3^-$-N removal efficiency and $NH_4^+$-N generation ratio increased significantly with increasing SDBS concentration and working current density. Then, the energy utilization efficiency of the nitrate-to-ammonia process on $V_O$-NiFe-LDH/CF at different working current densities was calculated.[52,53] As shown in Fig. S29, the energy utilization efficiency of the nitrate-to-ammonia process on $V_O$-NiFe-LDH/CF exhibited a gradual increase with increasing current density, reaching a maximum of 42.8% at 10 mA $cm^{-2}$. A decrease in energy utilization efficiency was observed at 20 mA $cm^{-2}$, which can be attributed to increased HER *via* Tafel or Heyrovsky mechanisms at higher current densities, resulting in a more negative cathodic potential and reduced faradaic efficiency for nitrate reduction.[54] Therefore, a working current density of 10 mA $cm^{-2}$ was identified for subsequent electrolysis experiments to balance energy efficiency and nitrate removal performance. In addition, both $NO_3^-$-N removal efficiency and $NH_4^+$-N generation ratio remain above 90% as the initial pH increases from 5 to 9, indicating the robust applicability of the nitrate-to-ammonia process on $V_O$-NiFe-LDH/CF across a broader initial pH range (Fig. 5c and S30). As shown in Fig. 5d and S31, electrolysis experiments conducted at varying initial $NO_3^-$-N concentrations (25–100 mg $L^{-1}$) revealed that $NO_3^-$-N removal capacity decreased from 96.8% to 58% with increasing initial $NO_3^-$-N concentration. This observation can be attributed to the saturation of active sites on $V_O$-NiFe-LDH/CF, which limits nitrate adsorption and activation. These results indicate that the $V_O$-NiFe-LDH/CF cathode is preferentially effective for low-concentration

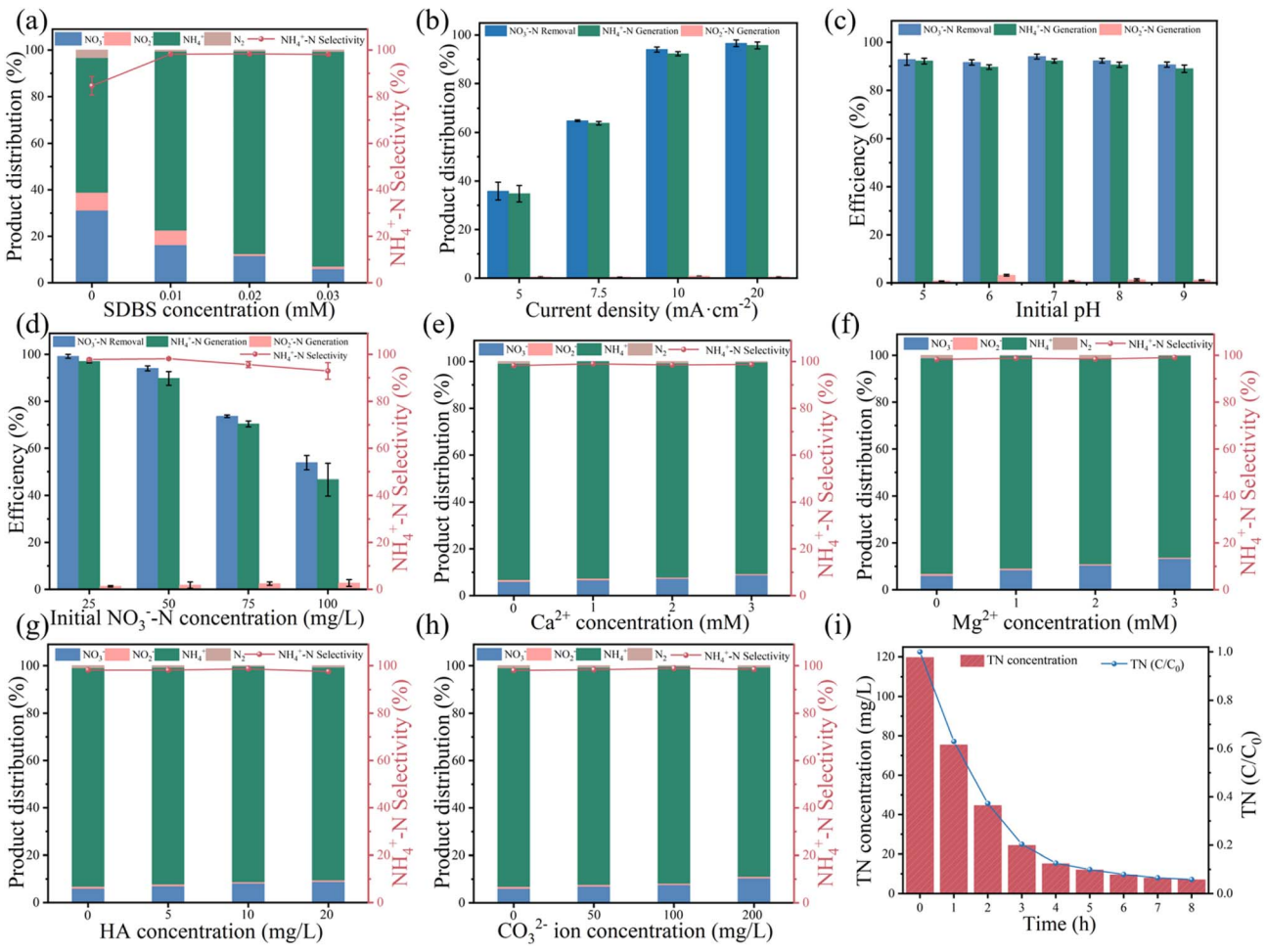


Fig. 5 (a–h) The effect of different operating parameters and interfering ions on electrochemical nitrate-to-ammonia by $V_O$-NiFe-LDH/CF. (i) Total nitrogen (TN) removal from practical industrial wastewater obtained using $V_O$-NiFe-LDH/CF.

nitrate-to-ammonia conversion in this system. Although the activity of $V_O$-NiFe-LDH/CF was suppressed at higher $NO_3^-$-N concentrations, ammonia remained high as the dominant product, highlighting its potential for direct application in low-concentration nitrate wastewater treatment. Considering the effects of various constituents in real wastewater,[55] electrolysis tests were conducted at the $V_O$-NiFe-LDH/CF cathode with different interfering ions at various concentrations. These results demonstrate minimal impact on catalytic performance (efficiency and selectivity) in this system, indicating the excellent stability of $V_O$-NiFe-LDH/CF for nitrate removal and ammonia conversion (Fig. 5e–h).

Indeed, ammonia recovery at low concentrations may lack economic feasibility compared to high-concentration recovery processes.[56] The treatment strategies for nitrate wastewater across different concentration ranges require in-depth consideration of "waste-to-wealth" and "waste-to-health" principles. Therefore, the subsequent conversion of generated $NH_4^+$-N to harmless $N_2$ assisted by chloride ions in wastewater aligns with human health and ecological sustainability goals.[57] The electrocatalytic performance of $V_O$-NiFe-LDH/CF was evaluated at different $Cl^-$ concentrations, as presented in Fig. S32. The $Cl^-$ addition significantly improves $N_2$ selectivity, which reaches 98.7% at a $Cl^-$ concentration of 1.5 g $L^{-1}$ under optimal conditions. In addition, the reaction was conducted under weakly alkaline conditions (pH 8–9), which has been demonstrated to effectively suppress the formation of highly toxic chloramines and favor their complete oxidation to $N_2$ through breakpoint chlorination.[58,59] Furthermore, the treatment ability of $V_O$-NiFe-LDH/CF for practical industrial nitrate-wastewater was evaluated at an initial total nitrogen (TN) concentration of 114.7 mg $L^{-1}$ (Fig. 5i), and the water quality parameters are provided in Table S1. The TN was reduced to blow 7 mg $L^{-1}$ through the synergistic effect of nitrate-to-ammonia conversion at the cathode and active chlorine species oxidation at the anode, achieving a TN concentration below the World Health Organization (WHO) emission limit standard.[60] Moreover, $Ca^{2+}$, $Mg^{2+}$ and chemical oxygen demand (COD) were efficiently removed during nitrate elimination, accompanied by significant chromaticity reduction in treated wastewater compared to the original sample (Fig. S33). Notably, $V_O$-NiFe-LDH/CF demonstrates a remarkable reduction in energy consumption for nitrate treatment (2.08 kWh $mol^{-1}$) compared with the other electrodes, as shown in Table S2.

## 4. Conclusion

In summary, this work presents a hydrophobic NiFe-LDH electrode formed by *in situ* electrochemical intercalation of SDBS. Different from traditional intercalation by the ion-exchange method, $V_O$-NiFe-LDH/CF not only retains the hydrophobic properties of SDBS but also induces rich oxygen vacancies. Structural characterization confirmed the successful synthesis of oxygen vacancy-rich, moderately hydrophobic LDH nanoflowers self-grown on copper foam. Electrochemical tests revealed that $V_O$-NiFe-LDH/CF accelerates the charge transfer kinetics. The $V_O$-NiFe-LDH/CF electrode exhibited a $NO_3^-$-N removal efficiency of 96.8% and an ammonia selectivity of 96% at an initial $NO_3^-$-N concentration of 50 mg $L^{-1}$, which is 2.1-fold higher than that of NiFe-LDH/CF. The enhanced nitrate electroreduction performance can be attributed to the optimized local electron structure and suppressed HER under low-concentration nitrate wastewater conditions. The hydrophobic surface suppresses the HER side reaction through repelling water molecules, while the introduction of oxygen vacancies modulates the local charge distribution of NiFe-LDH and reduced the energy barrier of hydrogenation. The Bode phase plots and EPR spectra show that $V_O$-NiFe-LDH/CF retains a good balance between generation and consumption of *H. Density functional theory (DFT) calculations revealed that the introduction of oxygen vacancies results in an optimized d-band center, enhanced nitrate adsorption and a reduced energy barrier for the rate-determining step (*NO to *NOH). Furthermore, the $V_O$-NiFe-LDH/CF electrode demonstrated outstanding long-term stability and robust anti-interference performance in cyclic durability tests and practical industrial wastewater treatment. This study provides a novel avenue to synthesize electrodes to realize the efficient treatment of low-concentration nitrate wastewater.

## Author contributions

Zhifeng Gao: formal analysis, investigation, methodology, writing – original draft. Jianxing Liang: formal analysis, investigation. Mingdi Sun: formal analysis, investigation. Xu Yin: investigation, methodology, supervision. Haojie Ling, methodology. Jiaxiu Wang, methodology. Kan Li: funding acquisition, writing – review and editing. Kajia Wei: funding acquisition, supervision, writing – review and editing. Weiqing Han: funding acquisition, supervision.

## Conflicts of interest

The authors declare that they have no known competing financial interests or personal relationships that could have appeared to influence the work reported in this paper.

## Data availability

Data are available from the corresponding author upon reasonable request.

Supplementary information (SI): additional experimental details including electrochemical measurements, DFT calculations, and catalyst characterization studies including SEM, XPS, *etc.* See DOI: https://doi.org/10.1039/d6sc02057g.

## Acknowledgements

This research was financed by the National Natural Science Foundation of China (No. 52070098, 52570084 & 52000104), the Jiangsu Province Carbon Peak Carbon Neutral Technology Innovation special fund project (BE2022861), the Youth Science and Technology Talent Lifting Project of Jiangsu Province (TJ-2023-099), the Natural Science Foundation of Shanghai (Grant

 

No. 25ZR1402228), the China Postdoctoral Science Foundation under Grant Number 2025M771245, and the Postdoctoral Fellowship Program of CPSF under Grant Number GZC20241003.

## References

1 K. Dong, S. Han, Y. Li, *et al.*, Testing, quantification, in situ characterization and calculation simulation for electrocatalytic nitrate reduction, *Nat. Protoc.*, 2025, **20**, 3678–3730, DOI: 10.1038/s41596-025-01289-8.

2 P. H. van Langevelde, I. Katsounaros and M. T. M. Koper, Electrocatalytic nitrate reduction for sustainable ammonia production, *Joule*, 2021, **5**(2), 290–294, DOI: 10.1016/j.joule.2020.12.025.

3 A. Seijas-Da Silva, A. Hartert, V. Oestreicher, *et al.*, Scalable synthesis of NiFe-layered double hydroxide for efficient anion exchange membrane electrolysis, *Nat. Commun.*, 2025, **16**(1), 6138, DOI: 10.1038/s41467-025-61356-2.

4 G. Fan, F. Li, D. G. Evans, *et al.*, Catalytic applications of layered double hydroxides: recent advances and perspectives, *Chem. Soc. Rev.*, 2014, **43**(20), 7040–7066, DOI: 10.1039/C4CS00160E.

5 K. Wang, R. Mao, R. Liu, *et al.*, Intentional corrosion-induced reconstruction of defective NiFe layered double hydroxide boosts electrocatalytic nitrate reduction to ammonia, *Nat. Water*, 2023, **1**(12), 1068–1078, DOI: 10.1038/s44221-023-00169-3.

6 J. Li, N. Zhao, X. Liu, *et al.*, Two-dimensional layered double hydroxides for advanced sensors, *Coord. Chem. Rev.*, 2025, **523**, 216262, DOI: 10.1016/j.ccr.2024.216262.

7 R. Yi, X. Mo, H. T. Yau, *et al.*, Interlayer expansion enables electrochemical domino C–N coupling for formaldoxime formation in aqueous media, *J. Am. Chem. Soc.*, 2025, **147**(36), 32809–32817, DOI: 10.1021/jacs.5c08836.

8 Y. Wang, Q. Pan, Y. Qiao, *et al.*, Layered Metal Oxide Nanosheets with Enhanced Interlayer Space for Electrochemical Deionization, *Adv. Mater.*, 2023, **35**(15), 2210871, DOI: 10.1002/adma.202210871.

9 S. Xu and C. Liu, Interface engineering gives enhanced selectivity in electrochemical nitrogen reduction reaction, *Chem Catal.*, 2022, **2**(8), 1841–1843, DOI: 10.1016/j.checat.2022.07.006.

10 J. Zhang, B. Zhao, W. Liang, *et al.*, Three-phase electrolysis by gold nanoparticle on hydrophobic interface for enhanced electrochemical nitrogen reduction reaction, *Adv. Sci.*, 2020, **7**(22), 2002630, DOI: 10.1002/advs.202002630.

11 Y. Xiong, Y. Wang, J. Zhou, *et al.*, Electrochemical nitrate reduction: ammonia synthesis and the beyond, *Adv. Mater.*, 2024, **36**(17), 2304021, DOI: 10.1002/adma.202304021.

12 W.-J. Sun, H.-Q. Ji, L.-X. Li, *et al.*, Built-in electric field triggered interfacial accumulation effect for efficient nitrate removal at ultra-low concentration and electroreduction to ammonia, *Angew. Chem., Int. Ed.*, 2021, **60**(42), 22933–22939, DOI: 10.1002/anie.202109785.

13 A. Li, Q. Cao, G. Zhou, *et al.*, Three-phase photocatalysis for the enhanced selectivity and activity of $CO_2$ reduction on a hydrophobic surface, *Angew. Chem., Int. Ed.*, 2019, **58**(41), 14549–14555, DOI: 10.1002/anie.201908058.

14 Y. Peng, L. Wang, Q. Luo, *et al.*, Molecular-level insight into how hydroxyl groups boost catalytic activity in $CO_2$ hydrogenation into methanol, *Chem*, 2018, **4**(3), 613–625, DOI: 10.1016/j.chempr.2018.01.019.

15 X. Wang, R. Zhang, C. Ma, *et al.*, Surface hydrophobic modification of MXene to promote the electrochemical conversion of $N_2$ to $NH_3$, *J. Energy Chem.*, 2023, **87**, 439–449, DOI: 10.1016/j.jechem.2023.08.043.

16 Y. Song, C. B. Musgrave, J. Su, *et al.*, Efficient $CO_2$-to-methanol electrocatalysis in acidic media via microenvironment-tuned cobalt phthalocyanine, *Nat. Nanotechnol.*, 2026, **21**, 78–86, DOI: 10.1038/s41565-025-02059-z.

17 Y. Liu, Y. Zheng, Y. Ren, *et al.*, Selective nitrate electroreduction to ammonia on CNT electrodes with controllable interfacial wettability, *Environ. Sci. Technol.*, 2024, **58**(16), 7228–7236, DOI: 10.1021/acs.est.4c01464.

18 D. Xu, Y. Liu, Y. Zhang, *et al.*, Fabrication of pyramid-$BiVO_4$/CdSe composite with controlled surface oxygen vacancies boosting efficient carriers' separation for photocathodic protection, *Chem. Eng. J.*, 2020, **393**, 124693, DOI: 10.1016/j.cej.2020.124693.

19 Y. Gao, K. Wang, C. Xu, *et al.*, Enhanced electrocatalytic nitrate reduction through phosphorus-vacancy-mediated kinetics in heterogeneous bimetallic phosphide hollow nanotube array, *Appl. Catal., B*, 2023, **330**, 122627, DOI: 10.1016/j.apcatb.2023.122627.

20 Y. Xu, C. Cheng, J. Zhu, *et al.*, Sulphur-boosted active hydrogen on copper for enhanced electrocatalytic nitrate-to-ammonia selectivity, *Angew. Chem., Int. Ed.*, 2024, **63**(16), e202400289, DOI: 10.1002/anie.202400289.

21 Y. Wu, M. Song, Y.-C. Huang, *et al.*, Promoting surface reconstruction of NiFe layered double hydroxides via intercalating $[Cr(C_2O_4)_3]^{3-}$ for enhanced oxygen evolution, *J. Energy Chem.*, 2022, **74**, 140–148, DOI: 10.1016/j.jechem.2022.06.045.

22 H. Bai, L. Liang, S. Chen, *et al.*, Modulating electronic structure of NiFe layered double hydroxide membrane by interlayer-confinement for enhanced water decontamination, *Appl. Catal. B Environ. Energy*, 2025, **363**, 124790, DOI: 10.1016/j.apcatb.2024.124790.

23 J. Zhang, X. Zhang, Z. Ma, *et al.*, POM-intercalated NiFe-LDH as enhanced OER catalyst for highly efficient and durable water electrolysis at ampere-scale current densities, *ACS Catal.*, 2025, **15**(8), 6486–6496, DOI: 10.1021/acscatal.5c00448.

24 X. Lin, Z. Wang, S. Cao, *et al.*, Bioinspired trimesic acid anchored electrocatalysts with unique static and dynamic compatibility for enhanced water oxidation, *Nat. Commun.*, 2023, **14**(1), 6714, DOI: 10.1038/s41467-023-42292-5.

25 Y. Liu, G. Chen, R. Ge, *et al.*, Construction of CoNiFe trimetallic carbonate hydroxide hierarchical hollow microflowers with oxygen vacancies for electrocatalytic

water oxidation, *Adv. Funct. Mater.*, 2022, **32**(32), 2200726, DOI: 10.1002/adfm.202200726.

26 K. Liang, Z. Dou, Y. Zhang, *et al.*, Preparation of one-step organic anion-modified MgAl-LDH films under mild conditions for Mg alloy corrosion protection, *J. Mater. Sci.*, 2023, **58**(43), 16841–16854, DOI: 10.1007/s10853-023-09070-6.

27 D.-Y. Wang, F. R. Costa, A. Vyalikh, *et al.*, One-step synthesis of organic LDH and its comparison with regeneration and anion exchange method, *Chem. Mater.*, 2009, **21**(19), 4490–4497, DOI: 10.1021/cm901238a.

28 Y. Sun, K. Fan, J. Li, *et al.*, Boosting electrochemical oxygen reduction to hydrogen peroxide coupled with organic oxidation, *Nat. Commun.*, 2024, **15**(1), 6098, DOI: 10.1038/s41467-024-50446-2.

29 D. Chen, S. Zhang, X. Bu, *et al.*, Synergistic modulation of local environment for electrochemical nitrate reduction via asymmetric vacancies and adjacent ion clusters, *Nano Energy*, 2022, **98**, 107338, DOI: 10.1016/j.nanoen.2022.107338.

30 J. Bao, X. Zhang, B. Fan, *et al.*, Ultrathin spinel-structured nanosheets rich in oxygen deficiencies for enhanced electrocatalytic water oxidation, *Angew. Chem., Int. Ed.*, 2015, **54**(25), 7399–7404, DOI: 10.1002/anie.201502226.

31 L. Liu, Q. Liu, Y. Wang, *et al.*, Nonradical activation of peroxydisulfate promoted by oxygen vacancy-laden NiO for catalytic phenol oxidative polymerization, *Appl. Catal., B*, 2019, **254**, 166–173, DOI: 10.1016/j.apcatb.2019.04.094.

32 G. Long, A. Wang, X. Liu, *et al.*, Tunable oxygen vacancy clusters enhanced catalytic activity of $CeO_2$ nanorods on $CO_2$ cycloaddition, *Angew. Chem., Int. Ed.*, 2025, **64**(34), e202508217, DOI: 10.1002/anie.202508217.

33 K. Flores, D. Varda, N. Hald, *et al.*, Engineering copper supported mixed manganese oxides as selective bimetallic electrocatalyst for nitrate to ammonia conversion at environmentally relevant concentrations, *Appl. Catal. B Environ. Energy*, 2025, **362**, 124682, DOI: 10.1016/j.apcatb.2024.124682.

34 K. Zhang, X. Zhu, N. Graham, *et al.*, Identification of dual center in self-supported Pd-dispersed $Cu_2O$/Cu nanowire arrays featuring cooperativity for durable electrochemical removal of low-concentration nitrate, *Appl. Catal. B Environ. Energy*, 2026, **384**, 126166, DOI: 10.1016/j.apcatb.2025.126166.

35 J. Zhang, L. Liu, N. Hu, *et al.*, Accelerating proton coupled electron transfer by confined Cu-Ni bimetallic clusters for boosting electrochemical hydrodeoxygenation of nitrate, *Appl. Catal. B Environ. Energy*, 2025, **371**, 125195, DOI: 10.1016/j.apcatb.2025.125195.

36 W. Kang, L. Yan, J. Tang, *et al.*, Electrochemical activation of graphite electrode for nitrate reduction: Energetic performance and application potential, *Appl. Catal., B*, 2023, **329**, 122553, DOI: 10.1016/j.apcatb.2023.122553.

37 R. Mao, H. Zhu, K. Wang, *et al.*, Selective conversion of nitrate to nitrogen gas by enhanced electrochemical process assisted by reductive Fe(II)-Fe(III) hydroxides at cathode surface, *Appl. Catal., B*, 2021, **298**, 120552, DOI: 10.1016/j.apcatb.2021.120552.

38 Y.-J. Shih, Z.-L. Wu, C.-Y. Lin, *et al.*, Manipulating the crystalline morphology and facet orientation of copper and copper-palladium nanocatalysts supported on stainless steel mesh with the aid of cationic surfactant to improve the electrochemical reduction of nitrate and $N_2$ selectivity, *Appl. Catal., B*, 2020, **273**, 119053, DOI: 10.1016/j.apcatb.2020.119053.

39 G. A. Cerrón-Calle, A. S. Fajardo, C. M. Sánchez-Sánchez, *et al.*, Highly reactive Cu-Pt bimetallic 3D-electrocatalyst for selective nitrate reduction to ammonia, *Appl. Catal., B*, 2022, **302**, 120844, DOI: 10.1016/j.apcatb.2021.120844.

40 L. Cai, Y. Liu, J. Zhang, *et al.*, Unveiling the geometric site dependent activity of spinel $Co_3O_4$ for electrocatalytic chlorine evolution reaction, *J. Energy Chem.*, 2024, **92**, 95–103, DOI: 10.1016/j.jechem.2023.12.002.

41 T. Jin, J. Wang, Y. Gong, *et al.*, Mechanochemical-tuning size dependence of iridium single atom and nanocluster toward highly selective ammonium production, *Chem Catal.*, 2023, **3**(1), 100477, DOI: 10.1016/j.checat.2022.11.016.

42 S. Liang, X. Teng, H. Xu, *et al.*, H* Species Regulation by Mn-$Co(OH)_2$ for Efficient Nitrate Electro-reduction in Neutral Solution, *Angew. Chem., Int. Ed.*, 2024, **63**(11), e202400206, DOI: 10.1002/anie.202400206.

43 Z. Fan, C. Cao, X. Yang, *et al.*, Interfacial Electronic Interactions Promoted Activation for Nitrate Electroreduction to Ammonia over Ag-Modified $Co_3O_4$, *Angew. Chem., Int. Ed.*, 2024, **63**(44), e202410356, DOI: 10.1002/anie.202410356.

44 J. Guan, L. Cai, W. Li, *et al.*, Boosting nitrate electroreduction to ammonia on atomic Ru-Co pair sites in hollow spinels, *Appl. Catal. B Environ. Energy*, 2024, **358**, 124387, DOI: 10.1016/j.apcatb.2024.124387.

45 J. Liang, K. Li, F. Shi, *et al.*, Constructing high-performance cobalt-based environmental catalysts from spent lithium-ion batteries: unveiling overlooked roles of copper and aluminum from current collectors, *Angew. Chem., Int. Ed.*, 2024, **63**(32), e202407870, DOI: 10.1002/anie.202407870.

46 H. Liu, S. Jia, L. Wu, *et al.*, Circumventing scaling relations via gradient orbital coupling promotes ammonia electrosynthesis on cobalt catalyst, *Angew. Chem., Int. Ed.*, 2025, **64**(32), e202510478, DOI: 10.1002/anie.202510478.

47 R. Javed, B. Zhao, Z. Zafar, *et al.*, Pd single-atoms doped $Cu_3P$ quantum dots with moderately optimized H* sorption behaviors for actualizing the multifunctional formaldehyde-nitrate galvanic system, *Adv. Mater.*, 2025, **37**(45), e12332, DOI: 10.1002/adma.202512332.

48 M. Xu, L. Huang, S. Zhang, *et al.*, Modulating electron transfer from palladium to spinel cobalt oxide nanofibers for high-efficiency hydrazine oxidation-assisted energy-saving nitrate-to-ammonia conversion, *Adv. Funct. Mater.*, 2026, **16**, e75722, DOI: 10.1002/adfm.75722.

49 Y. Yao, S. Zhu, H. Wang, *et al.*, A spectroscopic study on the nitrogen electrochemical reduction reaction on gold and platinum surfaces, *J. Am. Chem. Soc.*, 2018, **140**(4), 1496–1501, DOI: 10.1021/jacs.7b12101.

50 J.-Y. Fang, Q.-Z. Zheng, Y.-Y. Lou, *et al.*, Ampere-level current density ammonia electrochemical synthesis using CuCo nanosheets simulating nitrite reductase bifunctional nature, *Nat. Commun.*, 2022, **13**(1), 7899, DOI: 10.1038/s41467-022-35533-6.

51 B. Huang, J. Yan, Z. Li, *et al.*, Anode-electrolyte interfacial acidity regulation enhances electrocatalytic performances of alcohol oxidations, *Angew. Chem., Int. Ed.*, 2024, **63**(40), e202409419, DOI: 10.1002/anie.202409419.

52 L. Szpyrkowicz, S. Daniele, M. Radaelli, *et al.*, Removal of $NO_3^-$ from water by electrochemical reduction in different reactor configurations, *Appl. Catal., B*, 2006, **66**(1), 40–50, DOI: 10.1016/j.apcatb.2006.02.020.

53 L. Su, K. Li, H. Zhang, *et al.*, Electrochemical nitrate reduction by using a novel $Co_3O_4$/Ti cathode, *Water Res.*, 2017, **120**, 1–11, DOI: 10.1016/j.watres.2017.04.069.

54 R. Mao, C. Huang, X. Zhao, *et al.*, Dechlorination of triclosan by enhanced atomic hydrogen-mediated electrochemical reduction: Kinetics, mechanism, and toxicity assessment, *Appl. Catal., B*, 2019, **241**, 120–129, DOI: 10.1016/j.apcatb.2018.09.013.

55 J. Fan, L. K. Arrazolo, J. Du, *et al.*, Effects of ionic interferents on electrocatalytic nitrate reduction: mechanistic insight, *Environ. Sci. Technol.*, 2024, **58**(29), 12823–12845, DOI: 10.1021/acs.est.4c03949.

56 H. Huang, K. Peramaiah and K.-W. Huang, Rethinking nitrate reduction: redirecting electrochemical efforts from ammonia to nitrogen for realistic environmental impacts, *Energy Environ. Sci.*, 2024, **17**(8), 2682–2685, DOI: 10.1039/D4EE00222A.

57 P. Jiang, T. Zhou, J. Bai, *et al.*, Nitrogen-containing wastewater fuel cells for total nitrogen removal and energy recovery based on Cl·/ClO· oxidation of ammonia nitrogen, *Water Res.*, 2023, **235**, 119914, DOI: 10.1016/j.watres.2023.119914.

58 M. Duca and M. T. M. Koper, Powering denitrification: the perspectives of electrocatalytic nitrate reduction, *Energy Environ. Sci.*, 2012, **5**(12), 9726–9742, DOI: 10.1039/C2EE23062C.

59 A. G. Vlyssides, P. K. Karlis, N. Rori, *et al.*, Electrochemical treatment in relation to pH of domestic wastewater using Ti/Pt electrodes, *J. Hazard. Mater.*, 2002, **95**(1), 215–226, DOI: 10.1016/S0304-3894(02)00143-7.

60 J. Chen, H. Wu, H. Qian, *et al.*, Assessing nitrate and fluoride contaminants in drinking water and their health risk of rural residents living in a semiarid region of northwest china, *Exposure Health*, 2017, **9**(3), 183–195, DOI: 10.1007/s12403-016-0231-9.